Title: Low Frequency Plasmaspheric Hiss Wave Activity Parameterized by Plasmapause Location: Models and Simulations

Authors: A. A. Saikin[1], A. Y. Drozdov[1], D. M. Malaspina[2,3]

[1]Department of Earth, Planetary, and Space Sciences, University of California, Los Angeles, CA, USA

[2]Astrophysical and Planetary Sciences Department, University of Colorado Boulder, Boulder, CO, USA

[3]Laboratory for Atmospheric and Space Physics, University of Colorado Boulder, Boulder, CO, USA

Mailing Address[1]: The Geology Building, 595 Charles E. Young Drive East, Los Angeles, CA 90095

Key Points

1. Low frequency (20 -150 Hz) plasmaspheric hiss waves are modeled with respect to plasmapause location and distance from the plasmapause.

2. The plasmapause location-based hiss wave modeling produces smaller lifetimes for ~ 300 keV – 4 MeV electrons.

3. 3D simulations performed with this method yield more accurate results than L-based hiss wave modeling.

AGU Index Terms:

2730 Magnetosphere: Inner

2768 Plasmasphere

2774 Radiation Belts

2772 Plasma waves and instabilities

2722 Forecasting?

Running Title: Saikin et al., Low Frequency Hiss

Abstract: Plasmaspheric hiss waves are a dominant source of scattering for keV – MeV radiation belt electrons within the plasmasphere. Previous simulation and modeling work concerning hiss waves has often incorporated them via particle-based parameterizations (e.g., L-shell). However, recent work has shown that not only is hiss wave power loosely dependent on L-shell, but that proximity to the plasmapause may yield more accurate wave power distributions as it pertains to the modeling and scattering of electrons. This work serves to expand upon those previous studies by creating a low frequency (20 – 150 Hz) hiss wave model and incorporating a previously crafted high frequency (> 150 Hz) hiss wave model based on plasmapause location, proximity to the plasmapause, and *Kp* activity level. Diffusion coefficients created using this method produced shorter lifetimes for electrons between ~300 keV – 4 MeV than their L-sorted

counterparts. Furthermore, 3D-simulations using and comparing the different hiss wave models (plasmapause sorting vs. L-sorting) find that the plasmapause based approach yields more accurate results when compared to Van Allen Probe-A observations.

1. Introduction

Plasmaspheric hiss waves play a critical role in the dynamics of Earth's inner radiation belt electron population. Through wave particle-interactions, hiss waves scatter keV – MeV electrons in pitch angle, primarily inside or near the plasmapause, causing them to precipitate to Earth's atmosphere. Therefore, plasmaspheric hiss waves as a loss mechanism are an important component for simulations of inner radiation belt electrons (Albert et al., 2009; Fok et al., 2014; Miyoshi et al., 2006; Y. Y. Shprits et al., 2008; Subbotin & Shprits, 2009; Summers et al., 2007). When included in simulations, hiss wave activity is typically incorporated using statistically determined characteristics (e.g., spectral shape, intensity, frequency range, etc.) parameterized by magnetic local time (MLT), geomagnetic activity level, and by L shell (Glauert et al., 2014; K. Orlova et al., 2016; Ksenia Orlova & Shprits, 2014; Tsurutani et al., 2015).

However, recent studies have revealed that the distribution of hiss wave activity and wave power are largely dictated with respect to the location of the plasmapause (Malaspina et al., 2016, 2017) with peak hiss wave intensity found to occur consistently between 1 – 1.5 L shell earthward of the plasmapause. The distribution of hiss wave power with respect to distance from the plasmapause alters their corresponding diffusion coefficients, impacting the scattering of keV – MeV electrons. One-dimensional modeling of an idealized geomagnetic storm at $L = 3.5$ found that the plasmapause sorted hiss wave activity yielded faster decay times of 1 MeV electrons compared to their L-sorted counterparts (Malaspina et al., 2020). This result has critical implications for how hiss wave activity is incorporated into inner magnetosphere radiation belt modeling.

However, *Malaspina et al.* [2020] only performed a series of one-dimensional simulations (without comparisons to observations) and incorporated hiss wave activity observed between 150 – 2000 Hz, despite the existence of a low- frequency hiss component found between 40 – 150 Hz (Li et al., 2013; Malaspina et al., 2017). To determine the importance of a plasmapause-sorted hiss wave parameterization, we must expand upon the previous studies, which used only high frequency (150 – 2000 Hz) hiss, and include the low frequency component (like the previous L sorted counterparts (K. Orlova et al., 2016; Ksenia Orlova & Shprits, 2014; Spasojevic et al., 2015; Zhu et al., 2019)) while performing a series of three-dimensional simulations of radiation belt electrons and comparing their results to observed

radiation belts. This paper uses the same L_{pp} sorting metric as Malaspina et al. (2020) and Malaspina et al. (2016) to construct a low-frequency plasmaspheric hiss model and parameterization, developing corresponding diffusion coefficients, and testing them by performing radiation belt simulations.

This current study will be presented in the following manner: Section 2 will focus on the description of the instrumentation used to perform this study (the Van Allen Probes, Section 2.1), the methodology used to extract the hiss wave measurements from the Van Allen Probes (Section 2.2), the development of the hiss wave diffusion coefficients (Section 2.3), and a description of the Versatile Electron Radiation Belt (VERB) code used to simulate the radiation belts (Section 2.4). In Section 3, we will explore the method of how we parameterized the low-frequency hiss waves. Section 4 will focus on the VERB code simulations and results. In Section 5, we will discuss the implications of our results and present our conclusions, respectively.

1. Methodology

(a) Van Allen Probes

For this study, we use observations from the Van Allen Probes, two identical spacecraft which orbited the Earth with apogee and perigee of 5.8 and 1.1 R_e, respectively. The Probes (denoted as Probe-A and Probe-B) executed highly elliptical, low-inclination (~10°) orbits with a ~9-hour orbital period. Both probes were equipped with the Electric and Magnetic Field Instrument Suit and Integrated Science (EMFISIS) (Kletzing et al., 2013) with high temporal resolution magnetic field measurements (64 vectors per second), and the Electric Fields and Waves instrument (Wygant et al., 2013), which measured the spacecraft floating potential. Floating potential measurements, calibrated against measurements of the upper hybrid line by EMFISIS, are used to determine the in-situ total plasma density. Plasma measurements were made by the Radiation Belt Space Probes Energetic Particle Composition and Thermal Plasma suite (RBSP-ECT) (Spence et al., 2013). From the RBSP-ECT suite, we use measurements taken by the Magnetic Electron Ion Spectrometer (MagEIS) (which measured 20 keV – 5.0 MeV energy electrons) (Blake et al., 2013) and the Relativistic Electron Proton Telescope (REPT) (which measured the 1.8 – 20 MeV energy electrons) (Baker et al., 2013). Observations from Van Allen Probe B from September 2012 to May 2018 are used in this study. Data recorded from September 2012 to May 2016 on Van Allen Probe A were also used. Data recoded after May 2016 on Van Allen Probe A were not used, as accumulated radiation damage endured by the spacecraft's electric fields sensor preamplifiers compromised their ability to accurately measure spacecraft potential (required to determine the electron density

in combination with the upper hybrid frequency (Jahn et al., 2020)) shortly after this date.

L-shell was determined using the Olson-Pfitzer quiet-time magnetic field model (Olson & Pfitzer, 1974) at any given spacecraft location and time. The Olson-Pfitzer model performs well at both low *L*-shells ($L < 4.5$, during geomagnetically active and quiet times) and at high *L*-shells ($L > 4.5$, during geomagnetically quiet times). Since plasmaspheric hiss wave activity is within the plasmasphere regardless of the plasmapause location (with regards to L-shell), the Olson-Pfitzer model is an appropriate choice for plasmaspheric hiss studies.

1. **Plasmaspheric Hiss Data and Identification**

Following the method described in *Malaspina et al.*, (2016), plasma density was derived from the spacecraft potential measurements and calibrated for each orbit, against the measured upper hybrid frequency. Plasmapause crossings were determined whenever changes in density of 5 times (or higher) over 0.5 *L*-shells occurred (Moldwin et al., 2002). Should multiple density gradients with this criterion occur over a single inbound/outbound pass, the one closest to Earth was designated as the plasmapause crossing.

A series of exclusions were implemented to remove other phenomenon observed by the Van Allen Probes. First, data recorded at $L < 1.6$ were not considered. Half orbits where no plasmapause crossing were detected using the *Moldwin et al.* (2002) method were also excluded since the ΔL_{pp} (distance in *L*-shell from the plasmapause) could not be identified. Since we are trying to isolate the contribution of low-frequency hiss, only wave power observed between 20 – 150 Hz were considered. Wave observations outside of the identified plasmapause L shell (or when the corresponding plasma density was less than 50 cm^{-3}) are excluded as a filter against chorus wave power.

Further filters were applied to the remaining spectral wave data to isolate plasmaspheric hiss waves from other wave modes and background noise. Spectral bins where magnetosonic waves are dominant were removed (by time and frequency bin) by employing a compressibility threshold of $\frac{B_{wave\parallel}}{B_{\text{wave total}}} > 0.6$. Remaining spectral data was then subject to the following criteria to identify hiss waves: ellipticity > 0.7, signal to noise 5, and planarity > 0.2.

After the above-described filtering processes, plasmaspheric hiss data (in units of nT^2/Hz) were examined and binned with respect to distance of the plasmapause from the Earth (L_{pp}), frequency (using the EMFISIS frequency bins), distance to the plasmapause (ΔL_{pp}),

magnetic local time (MLT), and the Kp geomagnetic index. Four bins were used to describe L_{pp}: 2 $L_{pp} < 3$, 3 $L_{pp} < 4$, 4 $L_{pp} < 5$, and 5 $L_{pp} < 6$. Twenty-five bins (of 0.2 L) were used to describe the ΔL_{pp} (spanning a range of -5.0 to 0). Kp was divided into 6 "activity levels": 0 $Kp < 1$, 1 $Kp < 2$, 2 $Kp < 3$, 3 $Kp < 4$, 4 $Kp < 5$, and Kp 5 (the size of this last bin was chosen to ensure enough data for meaningful statistics, as intense geomagnetic conditions during the Van Allen Probes era were rare (Malaspina et al., 2020; Saikin et al., 2021)).

1. **Calculation of Diffusion Coefficients**

The Full Diffusion Code (FDC) (Shprits & Ni, 2009) is used to calculate the low-frequency hiss diffusion coefficients. The L_{pp}-sorted low frequency hiss wave polynomials derived in Section 3 are used as frequency inputs into the FDC. Plasma number density is defined using the (Denton et al., 2006) model. Following (Glauert & Horne, 2005), the wave normal distribution is assumed to be a Gaussian distribution with a peak of tan(0°), a width of tan(30°), and a lower (upper) cutoff at tan(0°) (tan(45°), respectively). Resonance orders from -5 to 5 (including a zero order) are also considered.

1. **The VERB code**

The VERB code models the relativistic electrons within the radiation belts by repeatedly solving the Fokker-Planck equation numerically (Shprits et al., 2008; Subbotin, Shprits, Gkioulidou, et al., 2011). The Fokker-Planck equation incorporates several processes to describe the dynamics and evolution of radiation belt electrons. For example, wave-particle interactions (i.e., local acceleration, radial transport, or electron loss to the atmosphere) caused by lightning whistler waves, electromagnetic ion cyclotron waves, chorus, or plasmaspheric hiss often impact radiation belt electrons through a combination of pitch-angle, energy, mixed term diffusion, and radial diffusion (caused by ultralow frequency (ULF) waves).

We use a single grid configuration of modified adiabatic invariants K ($K = \frac{J}{\sqrt{8m_0\mu}}$, where and m_0 represent the first adiabatic invariant and the electron mass, respectively) and V ($V = \mu * (K+0.5)^2$) to solve the 3-D Fokker-Planck equation (Landis et al., 2022; Saikin et al., 2021; Subbotin & Shprits, 2012). The use of these parameterizations is convenient for numerical calculations and defining boundary conditions because V is only loosely dependent on the particle's pitch angle, and K is independent of the particle's energy. This method allows us to sidestep the interpolation between numerical grids used in earlier VERB-3D simulations, which reduces unstable code behavior and numerical errors (Subbotin & Shprits, 2009). Using these modified invariants, the Fokker-Planck equation takes the form:

$$\frac{\mathrm{df}}{\mathrm{dt}} = \frac{1}{G}\frac{\partial}{\partial L}\mathrm{G}\ \langle D_{\mathrm{LL}}\rangle \frac{\partial f}{\partial L} + \frac{1}{G}\frac{\partial}{\partial V}G\left(\langle D_{\mathrm{VV}}\rangle \frac{\partial f}{\partial V} + \langle D_{\mathrm{VK}}\rangle \frac{\partial f}{\partial K}\right) + \frac{1}{G}\frac{\partial}{\partial K}G\left(\langle D_{\mathrm{KV}}\rangle \frac{\partial f}{\partial V} + \langle D_{\mathrm{KK}}\rangle \frac{\partial f}{\partial K}\right) - \frac{f}{\tau} \quad (1)$$

where f represents the three-dimensional phase space density (PSD), and is the electron's lifetime. Here, $\langle D_{\mathrm{LL}}\rangle$, denotes the radial diffusion coefficients while $\langle D_{\mathrm{VV}}\rangle$,$\langle D_{\mathrm{KK}}\rangle$, *and* $\langle D_{\mathrm{VK}}\rangle$ represent the drift and bounce-averaged diffusion coefficients. The Jacobian transformation from an adiabatic invariant system (, J, Φ) is denoted by G ($G = -2\pi B_0 R_E^2 L^{-2}\sqrt{8\mu m_0}/(K+0.5)^2$). R_E represents the Earth radius and $B_0 = 0.3$ G (the magnetic field on the equator of the Earth's surface). Finally, $f/$ is a loss term accounting for losses to the atmosphere and those caused by magnetopause shadowing.

In keeping with previous VERB-3D code simulation studies (Kim et al., 2011; Subbotin, Shprits, & Ni, 2011), we used the *Kp*-dependent electromagnetic ($\mathrm{DLL_m}$) radial diffusion coefficients derived from *Brautigam and Albert* (2000). Though initially designed for *Kp* 6, the functional dependence derived by Brautigam and Albert (2000) for the radial coefficient model has been used to include the $Kp > 6$ values.

All simulations were performed on an orthogonal grid of size 29 x 62 x 61 points for L^*, V, and K, respectively. The boundary conditions for these simulations are set at $L^* = 5.6$ (with the total L^* range set from 1.0 – 5.8) for energies from 10 keV to 10 MeV (V) and pitch angles from 0.7°–89.3° (K), respectively. The VERB code does not include convection since previous studies have shown that a lower energy boundary condition set at ~tens of keV have little effect on radiation belt electrons (Castillo et al., 2019; Subbotin, Shprits, Gkioulidou et al., 2011). Losses to the atmosphere are represented by setting the lower L^* boundary condition to zero. The L^* and pitch angle grid points are distributed linearly, while the V grid points are distributed on a logarithmic scale. The effective loss within the loss cone is simulated through the f/ term in Equation 1. The upper K boundary condition is set to both 0 and a zero-gradient PSD (representing a flat distribution at 90°), while the PSD at the lower K boundary is set to 0 (representing the losses to the atmosphere in the loss cone). PSD at the lower V boundary is set to an initial value and remains constant (representing the steady state balance between sources and losses of the low energy populations). PSD at the upper V boundary is set to 0.

Wave-particle interactions (through gyro resonance) are incorporated using previously derived parameterizations of waves: Very Low Frequency (VLF) whistler waves and lightning waves (Subbotin, Shprits, & Ni, 2011), dayside and nightside chorus waves (K. Orlova et al., 2016), and Electromagnetic Ion Cyclotron (EMIC)

waves (included when $Kp > 2$ and with a fixed amplitude, 0.1 nT^2) (Drozdov et al., 2017). The high-frequency component of plasmaspheric hiss waves is taken from Malaspina et al. (2020). For comparison, we have also utilized the plasmaspheric hiss model developed by Zhu et al. (2019). All diffusion coefficients used were converted to the modified adiabatic invariant coordinate system (V and K) using the methodology provided by Subbotin & Shprits (2012). The plasmapause boundary was modeled using the *Kp*-driven Carpenter & Anderson (1992) metric.

1. **Parameterizations of low-frequency hiss waves**

After hiss wave data were filtered and appropriately binned (according to Section 2.2), we employed another MLT categorization. While hiss wave activity is present throughout all MLT sectors, low frequency hiss waves exhibit stronger wave powers in the dayside magnetosphere (Malaspina et al., 2017), compared to the nightside. To ensure a more accurate parameterization, we have divided the low-frequency hiss waves into the "active" MLT sectors (7 MLT < 21) and the "non-active" sectors (21 MLT < 7). Figure 1 shows the wave power spectra (averaged for their respective bin) for all the active MLT low-frequency hiss wave spectra (independent of ΔL_{pp}, *Kp,* and L_{pp}). While all observed wave spectra decrease with decreasing frequency, from visual inspection, it becomes clear that there are at least two dominant spectral shapes. First, the wave spectra beginning at $> 10^{-2}$ nT^2 at ~142 Hz (i.e., the yellow and gold lines) immediately begin decreasing with sharper slopes. Wave spectra which generally begin at either 10^{-2} nT^2 (i.e., the cyan and blue lines) remain constant in power (140 - ~70 Hz) before they begin to noticeably decrease. Hiss wave profiles in Figure 1 have been sorted with respect to at what frequency they cross the wave power threshold (with each spectra being represented by a singular color).

Figure 1. All "Active" MLT Hiss Spectra vs Frequency

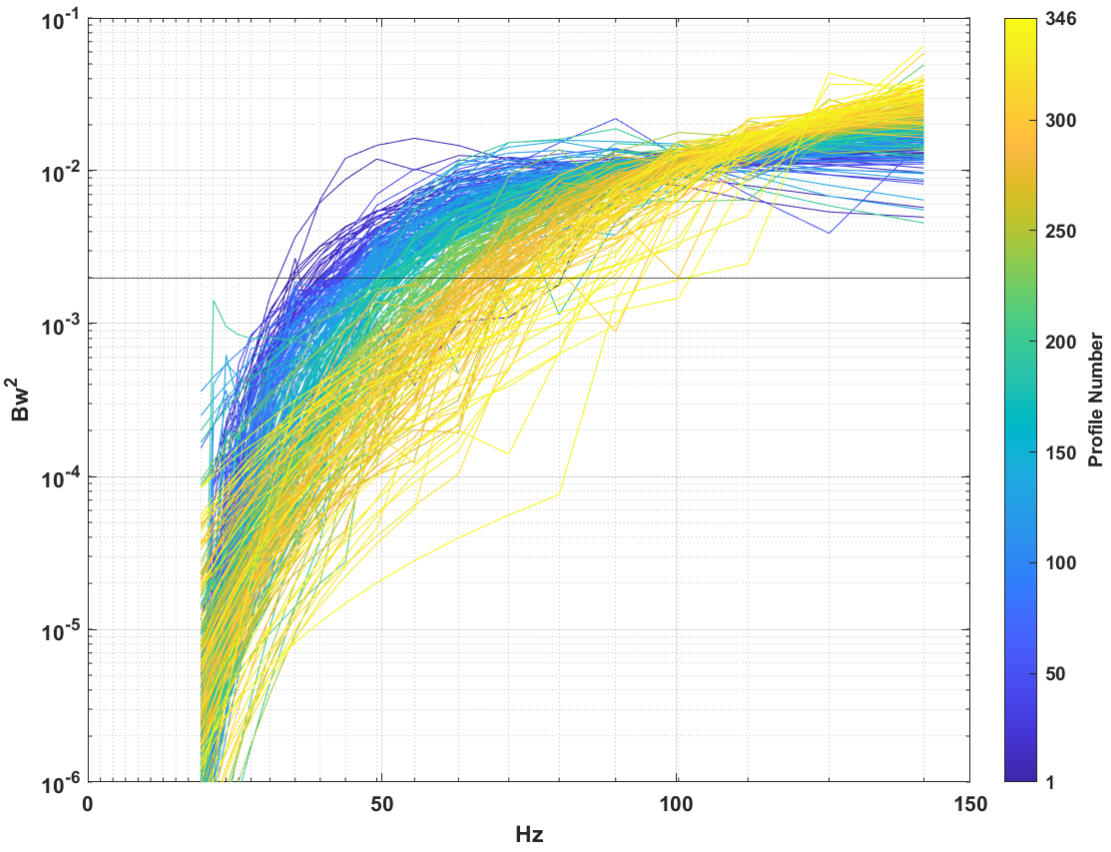

Figure 1: The wave spectra (nT^2) for all "*active*" MLT hiss waves versus frequency. The spectra have been sorted (and colorized) with respect to at which frequency it crosses the wave power threshold condition ($10^{-2.7}$ nT^2). Each color refers to a specific hiss wave profile.

From this observation, we have chosen to parameterize wave spectra based at the frequency at which they cross a threshold wave power ($10^{-2.7}$ nT^2). Note that altering this wave power threshold would shuffle which spectra get grouped together and affect the model. This created eleven frequency categories which crossed the threshold wave power between 35 – 112 Hz. For each category, data points are averaged and fitted with a 7$^{\text{th}}$ order polynomial (in keeping with Malaspina et al. (2020)):

$$\mathrm{PSD}(f) = \sum_{n=0}^{7} a_n f^n \quad (2)$$

In situations where the Root Mean Square Error (RMSE) > 0.30, when compared to the averaged data, a k-means clustering analysis (Jin & Han, 2017) sorting filter was applied. A polynomial number was assigned for each sorted averaged spectrum (starting with the lowest frequency threshold crossing, i.e., 35 Hz). Figure 2 shows the frequency categories and the resulting derived polynomials for the active MLT sectors (for a total of 24 polynomials).

Figure 2. The "Active" MLT Derived Polynomials

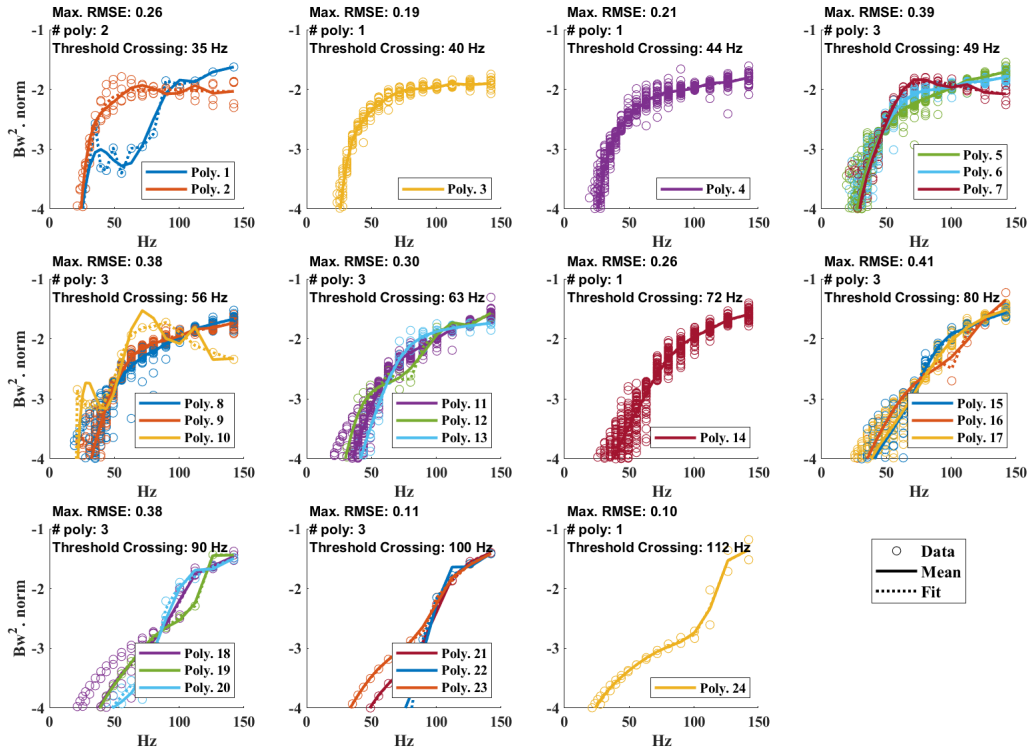

Figure 2: The 24 fitted "active" polynomials by their frequency threshold crossing and k-means filtering. For each polynomial: the data used to derive each polynomial (circle), their mean average (solid line), and their corresponding polynomial fit (dashed lines) are plotted. The max derived RMSE and the number of polynomials per frequency bin are also listed.

A similar process was used to examine the "non-active" hiss wave spectra (see Figure 3). However, due to the limited variability, the "non-active" hiss wave spectra were sorted into 3 spectral shapes (Freq. $<$ 56 Hz (non-active polynomial 1), 56 Hz $\leq$ Freq. $<$ 72 Hz (non-active polynomial 2), and 72 Hz $\leq$ Freq. (non-active polynomial 3)) (Figure 4). The coefficients for each respective polynomial can be found in the supplementary materials for the "active" and "non-active" polynomials, respectively.

Figure 3. All Non-active Hiss Spectra vs Frequency

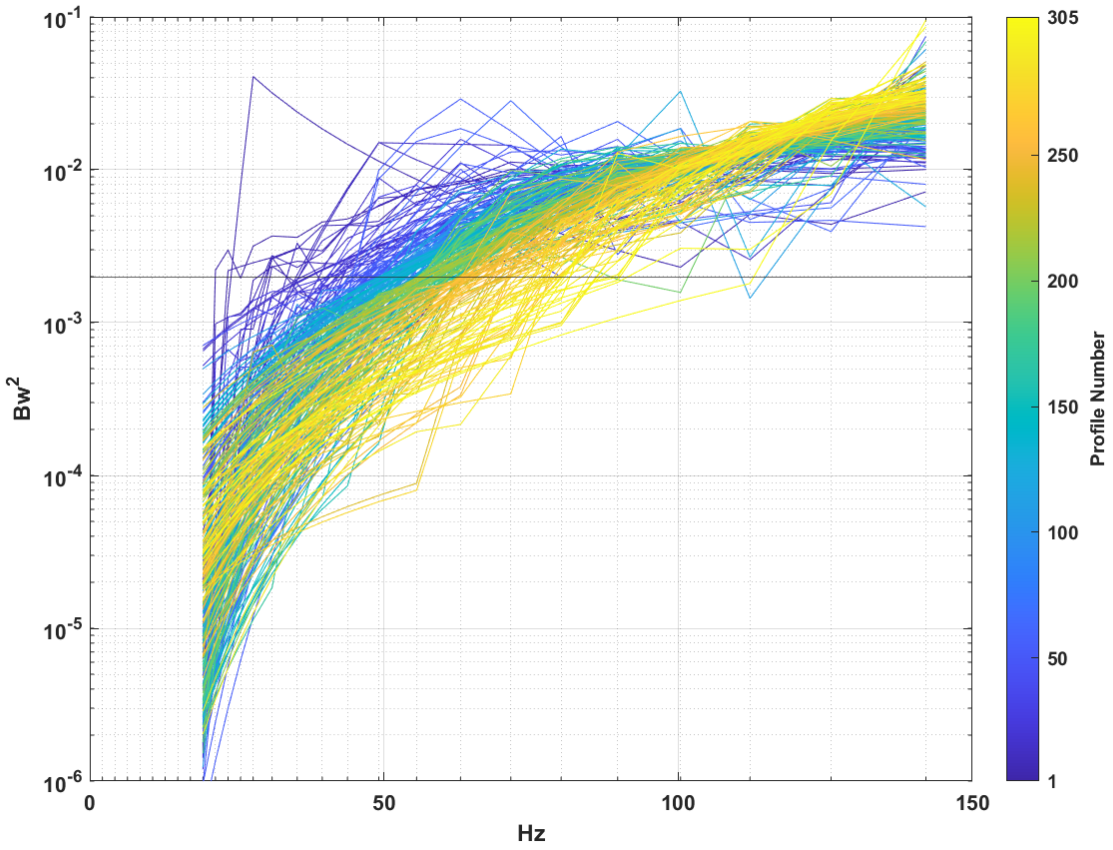

Figure 3: The wave spectra (nT^2) for all "*non-active*" MLT hiss waves versus frequency. The spectra have been sorted (and colorized) with respect to at which frequency it crosses the wave power threshold condition ($10^{-2.7}$ nT^2). Each color refers to a specific hiss wave profile.

Figure 4. The "Nonactive" Polynomials

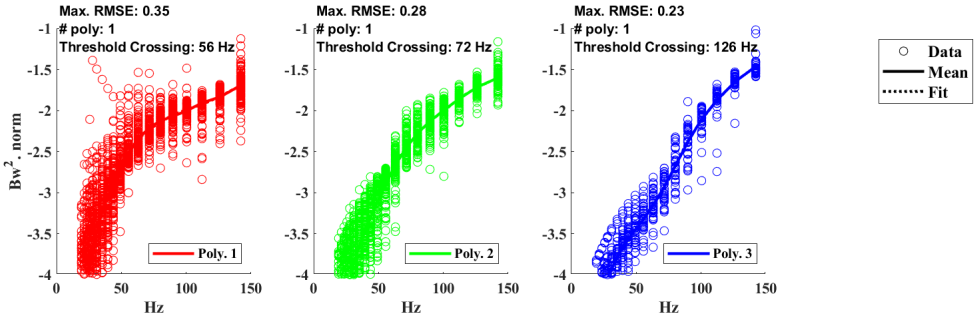

Figure 4: The 3 fitted "non-active" polynomials by their frequency cutoff. For each polynomial: the data used to derive each polynomial (circle), their mean average (solid line), and their corresponding polynomial fit (dashed lines) are plotted. The max derived RMSE and the number of polynomials per frequency bin are also listed.

With the 27 unique polynomials, we can describe the entire low-frequency hiss range by assigning the appropriate polynomial to the hiss wave spectra observed at that L_{pp}, ΔL_{pp} and Kp activity level. The appropriate "active" and "non-active" polynomials are then weighted (by MLT coverage) and combined as:

$$PSD = \left(\frac{14}{24}\right) * Active\ Polynomial + \left(\frac{10}{24}\right) * Nonactive\ Polynomial \quad (3)$$

Figure 4 shows an example of how well this model performs. Panels a, d, g, and j show the Van Allen Probe observations of hiss wave power versus frequency in the indicated L_{pp} and ΔL_{pp} bins for Kp activity level 3. At 150 Hz, a horizontal line has been placed to distinguish the boundary between high- and low-frequency hiss wave activity. Panels b, e, h, and k showcase the low frequency (below the 150 Hz line) and the Malaspina et al. (2020) (above the 150 Hz line) models. Note that the scaling factors derived for Malaspina et al. (2020) polynomials have been modified to be consistent with the methods used in this study (e.g., data observations are binned by 1-hour in MLT instead of 4-hour MLT slices). The normalized difference between the Van Allen Probes observations and the entire model is shown in panels c, f, i, and j (along with the maximum and average normalized difference values). The comparisons at other Kp activity levels can be found within the supplementary materials (Figures S1-S5).

Figure 4. Comparison between Polynomials and Data observations, *Kp* activity level = 3

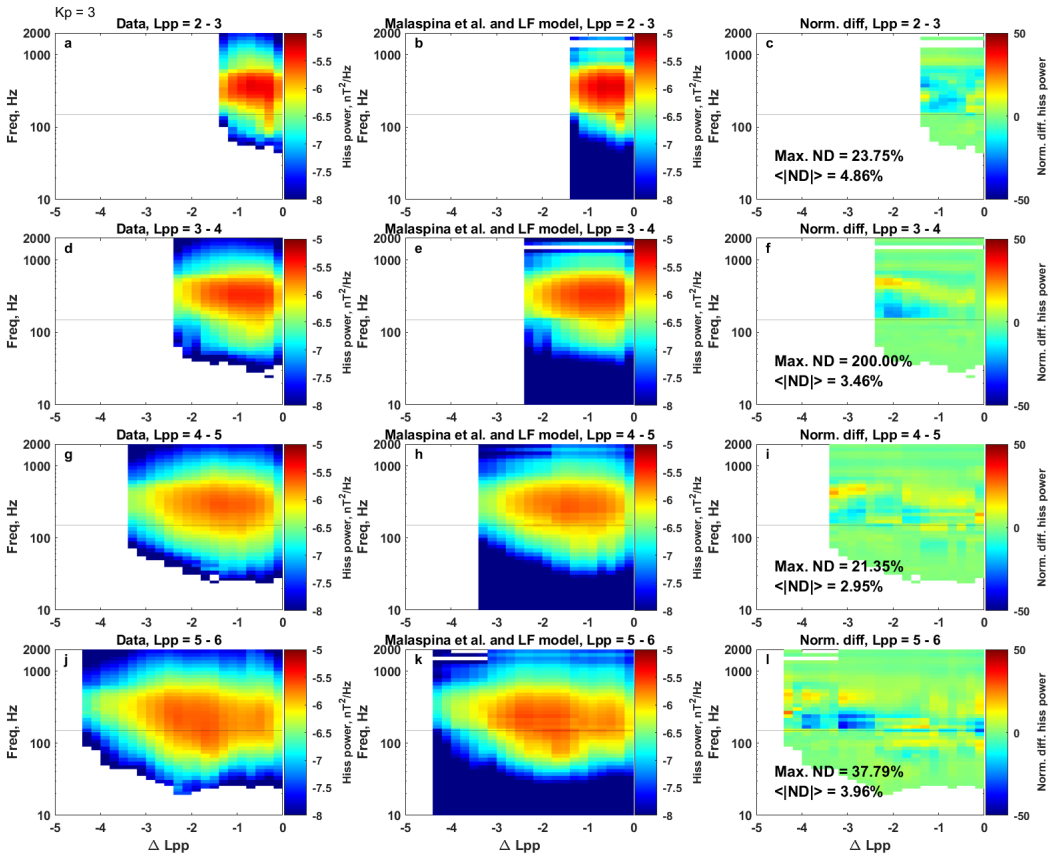

Figure 4: The Van Allen Probes observations of hiss wave power versus frequency (Panels a, d, g, and j) per L_{pp} and ΔL_{pp} bin for Kp activity level 3. Panels b, e, h, and k show the Malaspina et al. (2020) Hiss wave model results (above the 150 Hz line) and the modeled low-frequency hiss wave power (below the 150 Hz line). The normalized difference (including the maximum and average normalized difference) is shown on panels e, f, i, and j.

Overall, the low-frequency hiss model closely models the Van Allen Probes observations. When considering all *Kp* activity levels (see Supporting Material Figures S1 - S5), the average normalized difference per L_{pp} bin stays below 9%, while only a handful of ΔLpp bins show large, normalized differences (i.e., $> 80\%$).

Using the FDC (see Section 2.3), the 27 "active" and "non-active" polynomials are used to derive a series of unique polynomial diffu-

sion coefficients. These diffusion coefficients are then organized and reassembled into the appropriate L_{pp}, ΔL_{pp}, and Kp bins based on the corresponding polynomial associated with that bin. To accommodate the entire range of hiss wave activity, these low-frequency hiss wave diffusion coefficients were added to the high-frequency hiss wave diffusion coefficients derived from Malaspina et al. (2020) to describe the entire frequency spectrum for hiss wave activity. This will be referred to as the combination of the Malaspina et al. (2020) and low-frequency hiss wave model or simply, the combination model. A sample diffusion coefficient comparison between the Malaspina et al. model the low frequency model, and the combination models can be seen in Figure 5.

Figure 5. Diffusion Coefficients example

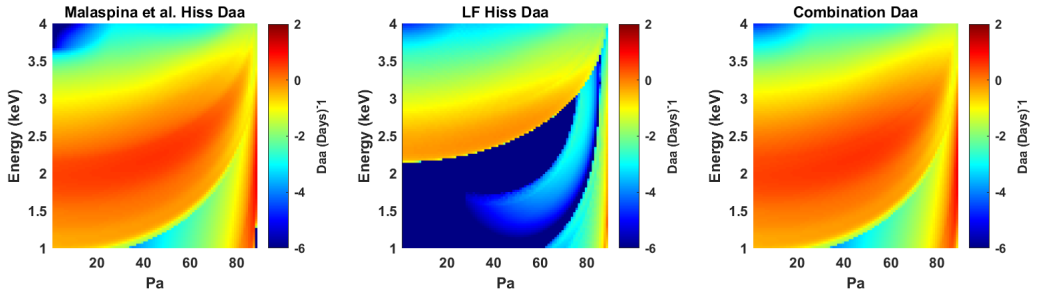

Figure 5: The D diffusion coefficients for the Malaspina et al. (2020) (left), the low frequency (middle), and the combination model (right) for the $L_{pp} = 5 - 6$, $L = 4.0$, Kp activity level = 2.

With the newly assembled hiss wave diffusion coefficients, we began exploring how the L_{pp} sorted method can scatter electrons by calculating the electron lifetime, $\tau = D_{\propto\propto}(\propto_{\mathrm{LC}})^{-1}$, where $\propto_{\mathrm{LC}}$ is the loss cone angle (Shprits et al., 2006). Figure 6 shows the electron lifetimes ( ) as a function of kinetic energy ($\mathrm{E_k}$) at $L = 3.2$, 3.4, 3.6, and 3.8 for Kp activity levels 1, 3, 4, and 5, respectively. Each plot features three different hiss wave methods: Zhu et al. (2019) in green; the Malaspina et al. (2020) in the blue-cyan colored lines; and the combination model in the red-orange lines. Note, multiple lines are shown for the Malaspina et al. (2020) and combination model to reflect the differences in plasmapause location, (e.g., "Mal. Lpp3" refers to the Malaspina et al. (2020) model when the plasmapause is located between 3 $\mathrm{L_{pp}} < 4$, etc.). See Supporting Materials, Figures S6 and S7, for lifetimes at other L shells.

Using this format, we noticed a major trend. First, at the lower energies, the Zhu et al. (2019) method tended to produce lifetimes around an order of magnitude shorter than Malaspina et al. (2020)

and the combination model. From 500 keV - ~4 MeV, the combination model produced the shortest lifetimes across all L_{pp}, L shells, and Kp activity levels. Occasionally the Malaspina et al. (2020) model also yielded shorter lifetimes than the Zhu et al. (2019) model (ex. Figure 6d, $L = 3.6$, Kp activity level 1). As the energy increases beyond 4 MeV, Zhu et al. (2019) produced the shortest lifetime. At energies $>$ ~100 keV and $<$ 4 MeV, the lifetimes for all three models exceed 10^2. At higher L shells (L $>$ 5) and Kp activity level $<$ 5, both the combination model and Zhu et al. (2019) model produced short lifetimes ($<$ ~10^0) at ~10 – 500 keV (see Figure S7 in the Supplementary Materials).

Figure 6. lifetimes

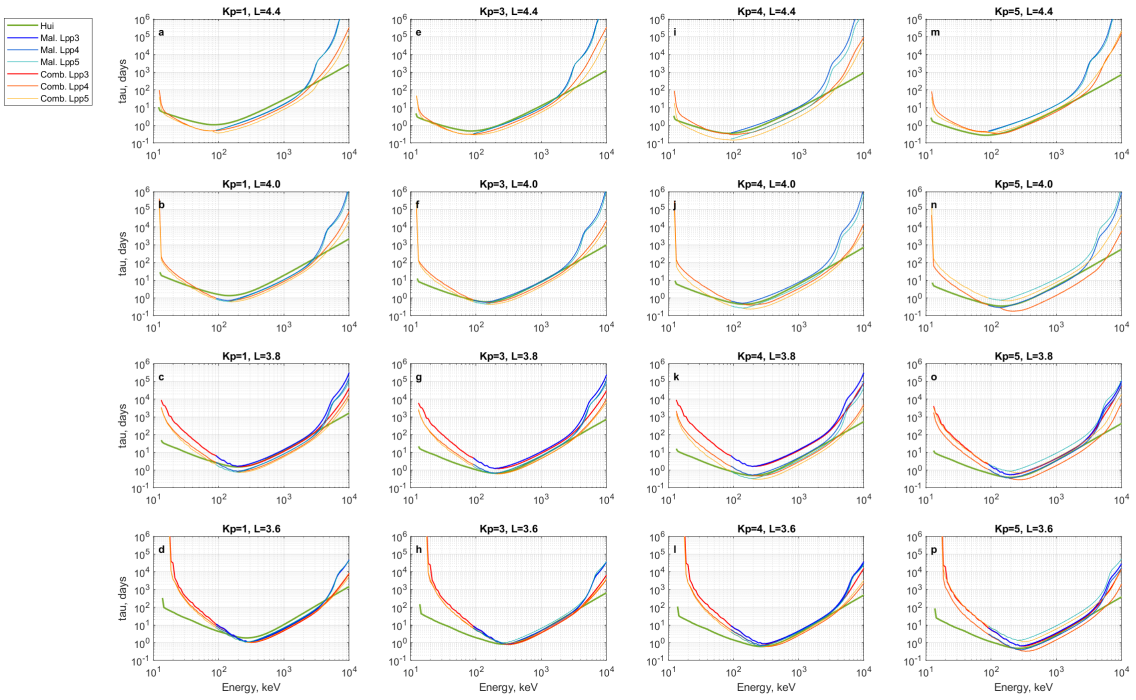

Figure 6: The lifetimes vs. energy for the hiss waves parameterized by Zhu et al. (2019) (green), the Malaspina et al. (2020) (blue and cyan), and the combination of Malaspina et al. (2020) with the low-frequency hiss (red and orange) for the selected L shells and Kp activity levels.

1. **VERB code simulation results**

Figure 7 shows a full VERB-3D simulation of the 1.0 MeV 75° pitch angle radiation belt electrons for the year 2013 between $L^* = 2.0$ – 5.6 using different hiss wave diffusion coefficients per simulation: a simulation without hiss wave (7b); a Zhu et al. (2019) hiss wave simulation (7d); the Malaspina et al. (2020) L_{pp} parameterized hiss waves (7f); and the combination of Malaspina et al. (2020) with low-frequency hiss (7h). The corresponding Van Allen Probe-A observations have been included (panel 7a). Panel 7a shows the *Kp* and L_{pp} during this period. Other select energies simulated (0.2 – 3.5 MeV) are included in supplementary materials (Figures S8 - S11).

To assess the accuracy of these simulations, we have calculated the normalized difference and log difference between the simulations and the Van Allen Probes observations. The normalized difference was calculated using:

$$\mathrm{ND}(L,t) = \frac{\mathrm{Flux}_{\mathrm{simulation}}(L,t) - \mathrm{Flux}_{\mathrm{Observed}}(L,t)}{\max(\mathrm{Flux}_{\mathrm{Observed}}(L{=}3.0 \ to \ L{=}5.6, \ t))} \quad (4)$$

while the log difference was calculated using:

$$\mathrm{LD}(L,t) = \log_{10}\left(\mathrm{Flux}_{\mathrm{simulation}}(L,t)\right) - \log_{10}\left(\mathrm{Flux}_{\mathrm{Observed}}(L,t)\right) \quad (5)$$

In Figure 7, for each corresponding simulation, we plotted the normalized difference and printed the mean normalized difference per simulation: No hiss (7c); Zhu et al. (2019) (7e); Malaspina et al. (2020) (7g); and the combination model (7i). For full L shell vs. time plot comparisons (like Figure 7), select figures for the log difference can be found within the supplementary materials (Figures S12 – S15). To simplify the results found within those figures, we calculated the mean normalized difference and log difference per energy and pitch angle (Figure 8). To avoid oversampling small values produced by the simulation and to focus on the radiation belts, we only included observations for L 3.0.

As expected, the complete exclusion of hiss wave activity (Figure 7b) did not produce enough scattering of MeV electrons, which resulted in the worst accuracy among the hiss wave parameterizations at most energies (Figure 8). The purely L parameterized hiss waves (Zhu et al., 2019) noticeably scattered more electrons within L=~2.5 – 3.5 (Figure 7c) compared to the no-hiss simulation. However, with the L_{pp} parameterized hiss wave models (Figures 7d and 7e), there are sharper pronounced slot regions (ex. $L^* = 3.2$ – 4.0 April 2013) produced which are not produced in the Zhu et al. (2019) simulation. These sharp losses more closely track with the Van Allen Probe-A observations. This is reflected in the mean normalized difference in Figure 8. Both the Malaspina et al. (2020) and the combination with low-frequency hiss have lower mean normalized

differences than the exclusively L^* parameterized hiss waves (especially at < 4 MeV and for pitch angle 60°). As energy increases and decreases beyond 4.0 and 0.4 MeV (respectively), the mean normalized difference across all four simulations (and pitch angles) begin to converge. As suggested by the increasing lifetimes (Figure 6), hiss does not contribute significantly to scattering at those energies.

Figure 7. The VERB-3D simulated 1.0 MeV 75° pitch angle radiation belt electrons.

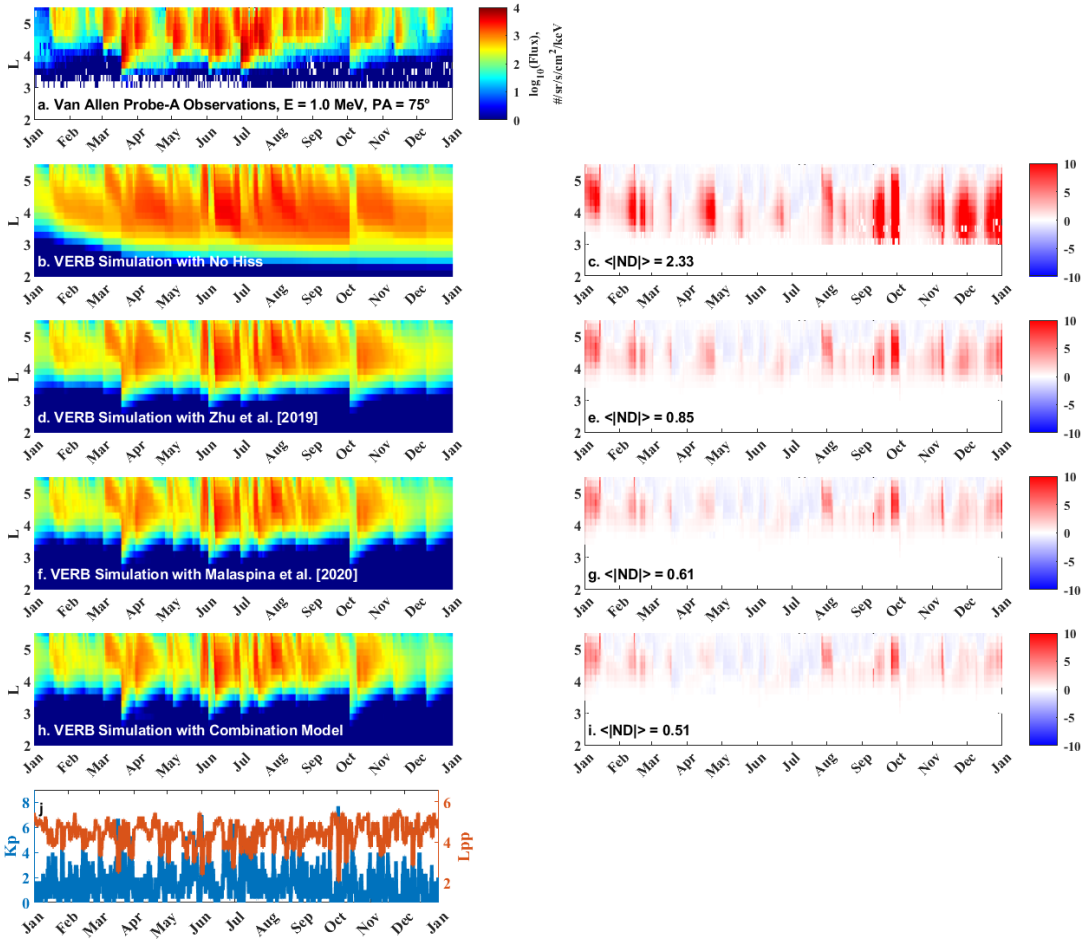

Figure 7: The 2013 Van Allen Probe-A observations of 1.0 MeV

75° pitch angle radiation belt electron flux (versus L^*) (a), and the corresponding simulated 1.0 MeV 75° pitch angle electron flux when using no hiss wave activity (b); Zhu et al. (2019) hiss wave model (d); the Malaspina et al. (2020) hiss wave model (f); the combination of Malaspina et al. (2020) and our low frequency hiss wave model (h). The normalized difference for each simulation is also plotted: No Hiss ©; Zhu et al. (2019) (e); Malaspina et al. (2020) (g); and the combination model (i). Finally, the Kp and plasmapause position are also plotted (j).

Figure 8. Mean Normalized and Log Difference vs. Energy

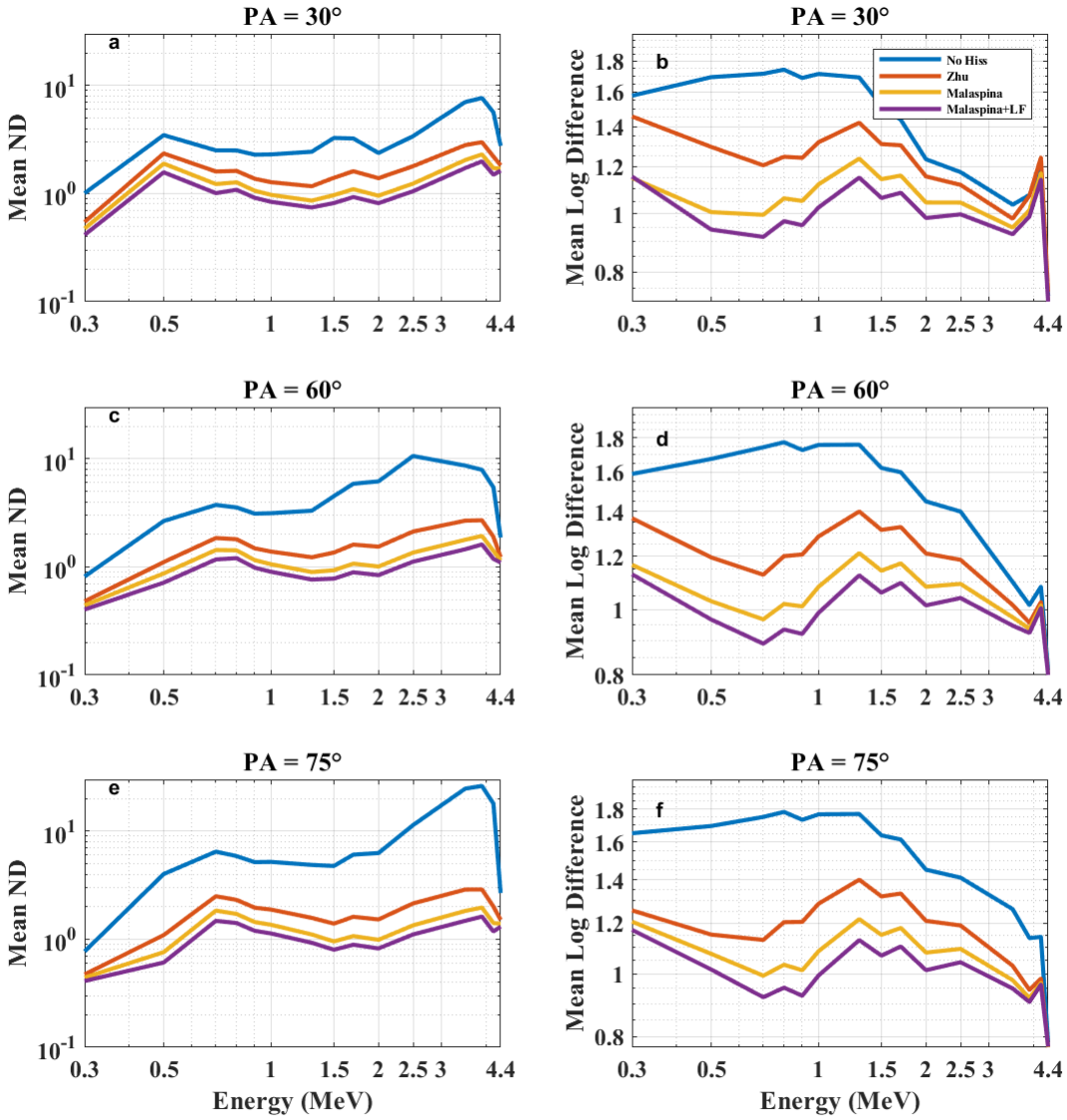

Figure 8: The mean normalized (a, c, e) and log difference (b, d, f) per energy for 30°, 60°, and 75° pitch angle electrons between Van Allen Probe-A observations and the corresponding hiss parameterization.

1. **Discussion and Summary**

This study utilized Van Allen Probes observations of low (20 – 150 Hz) frequency plasmaspheric hiss waves observed between 2012 – 2016, to develop a new empirical hiss wave model parameterized by plasmapause location (L_{pp} and ΔL_{pp}), MLT, and geomagnetic activity (i.e., Kp activity level). The twenty-seven unique polynomials (for both active and non-active MLT sectors) developed to describe the low-frequency hiss waves were used to derive a new set of plasmaspheric hiss wave diffusion coefficients. This work serves as an expansion upon Malaspina et al. (2017) and Malaspina et al. (2020), which focused on parameterizing hiss wave activity with respect to the plasmapause.

For energies 0.2 – 4.2 MeV (and pitch angles 30°, 60°, and 75°), a series of VERB-3D simulations were performed to examine how accurate each unique plasmaspheric hiss wave parameterization was to Van Allen Probe-A observations. The examples included: a simulation in which no hiss waves were included; an L^* parameterized description (Zhu et al., 2019) covering both low and high frequency hiss (20 - 2000 Hz); a plasmapause-based high frequency (> 150 Hz) hiss wave parameterization (Malaspina et al., 2020); and a combination of both high and low frequency plasmapause parameterized hiss wave parameterizations. When the results were compared among each simulation, the combination of high- and low-frequency hiss parameterized by plasmapause location yielded the most accurate results by normalized difference. For log difference, the combination modeled yielded the most accurate results between ~0.5 – 4.4 MeV, pitch angle 30° particles.

Beyond the 4.0 MeV, all four simulations converge with respect to mean normalized difference (Figure 8). This result was inferred with Figure 6, as beyond this range, the lifetimes rapidly increased (by 10^2 – 10^4, depending on which hiss wave model is used). The < 4.0 MeV energy range is when hiss wave-induced electron scattering is at its peak. Outside of these energies, other wave-particle interactions become the dominant form of electron scattering. For example, at > 4 MeV, EMIC waves become effective scattering mechanisms of electrons (e.g., Drozdov et al., 2017; Ni et al., 2015; Ni et al., 2018; Zhang et al., 2016).

While our combination plasmapause hiss wave model produced sharper slot regions which were more consistent with the Van Allen Probe-A observations, there still exist remanent belt structures at $L^* = \sim 3$ in the simulations (see Figures S8de and S11de in supplementary materials for examples). These remanent belts are not produced in the L^* parameterization by Zhu et al. (2019) (Figures S8b and S11b). This may be caused by how our method parameterized hiss wave power compared to Zhu et al. (2019).

While both Zhu et al. (2019) and the combination model both scale with respect to *Kp*, our wave power distribution differed with respect to L^*. For example, our hiss wave spectra at $L^* = 3.0$ when $L_{pp} = 3 - 4$ is not necessarily identical (i.e., a different active/non-active polynomial) to the hiss wave spectra at $L = 3.0$ when $L_{pp} = 4 - 5$. The Zhu et al. (2019) hiss wave model consists of a predefined parameterization in L shell that is scaled with respect to *Kp* (Spasojevic et al., 2015). This redistribution of hiss wave power may result in weaker electron scattering at low *Kp* values for our plasmapause-based hiss wave model compared to Zhu et al. (2019).

Since our simulations have become more accurate at reproducing observed electron fluxes by using the plasmapause related sorting, it may be worth re-examining other wave activity within this context. For example, lightning-generated whistler waves are also dominant at these energies and low L^* (Albert et al., 2020). Re-parameterizing lightning-generated whistlers using ΔL_{pp} may help improve our simulation results and scatter these low L^* remnant electrons. Future studies should consider re-evaluating these waves (e.g., lightning-generated whistlers, EMIC, etc.) within the context of their relationship to the plasmapause.

Acknowledgements

This research is supported by NASA award NSSC18K1034. Measurements from the Van Allen Probes Mission used in this study were obtained from the MagEIS and REPT data directories (https://www.rbsp-ect.lanl.gov/), the EMFISIS data directory (http://emfisis.physics. uiowa.edu) and the EFW data directory (http://www.space.umn.edu/rbspefw-data/). Historical *Kp* measurements were found at ftp://ftp.gfz-potsdam.de/ pub/home/obs/kp-ap/. Used diffusion coefficients and the codes are available at (ftp://rbm.epss.ucla.edu/). The data produced (e.g., Diffusion coefficients, PSD for the electron flux for the year 2013, polynomial coefficients) and their corresponding plotting scripts can be found at this location https://doi.org/10.25346/S6/FS9TDL (Polynomial coefficients), https://doi.org/10.25346/S6/FEXJOU (Malaspina et al. (2020) Diffusion Coefficients and updated scaling), https://doi.org/10.25346/S6/6VHDXS (PSD for The Combination Model simulation), https://doi.org/10.25346/S6/JBWI XY (PSD for the No Hiss Simulation), https://doi.org/10.25346/S6/AU1IZ2 (PSD for the Malaspina et al. (2020) simulation), https://doi.org/10.25346/S 6/3G3RL2 (PSD for the Zhu et al. (2019) simulation), https://doi.org/10.253 46/S6/Q2R5M0 (The Low Frequency Hiss Wave Diffusion Coefficients), https: //doi.org/10.25346/S6/J5HQNS (Matlab .fig files for all energies and pitch angles). This work used computational and storage services associated with the Hoffman2 Shared Cluster provided by UCLA Institute for Digital Research and Education's Research Technology Group. The authors would like to thank

Sharon Uy.

References

Albert, J. M., Meredith, N. P., & Horne, R. B. (2009). Three-dimensional diffusion simulation of outer radiation belt electrons during the 9 October 1990 magnetic storm. *Journal of Geophysical Research*, (114), 1–21.Albert, J. M., Starks, M. J., Selesnick, R. S., Ling, A. G., O'Malley, S., & Quinn, R. A. (2020). VLF Transmitters and Lightning-Generated Whistlers: 2. Diffusion of Radiation Belt Electrons. *Journal of Geophysical Research: Space Physics*, *125*(3), 2–15. https://doi.org/10.1029/2019ja027030Baker, D. N., Kanekal, S. G., Hoxie, V. C., Batiste, S., Bolton, M. K., Li, X., et al. (2013). The Relativistic Electron-Proton Telescope (REPT) Instrument on Board the Radiation Belt Storm Probes (RBSP) Spacecraft: Characterization of earth's radiation belt high-energy particle populations. *Space Sci Rev*, *9781489974*(179), 337–381. https://doi.org/10.1007/978-1-4899-7433-4-11Blake, J. B., Carranza, P. A., Claudepierre, S. G., Clemmons, J. H., Crain, W. R., Dotan, Y., et al. (2013). The magnetic electron ion spectrometer (MagEIS) instruments aboard the Radiation Belt Storm Probes (RBSP) spacecraft. *Space Science Reviews*, *179*(1–4), 383–421. https://doi.org/10.1007/s11214-013-9991-8Brautigam, D. H., & Albert, J. M. (2000). Radial diffusion analysis of outer radiation belt electrons during the October 9, 1990, magnetic storm. *Journal of Geophysical Research: Space Physics*, *105*(A1), 291–309. https://doi.org/10.1029/1999ja900344Carpenter, D. L., & Anderson, R. R. (1992). An ISEE/whistler model of equatorial electron density in the magnetosphere. *Journal of Geophysical Research*, *97*(A2), 1097–1108. https://doi.org/10.1029/91JA01548Castillo, A. M., Shprits, Y. Y., Ganushkina, N., Drozdov, A. Y., Aseev, N. A., Wang, D., & Dubyagin, S. (2019). Simulations of the inner magnetospheric energetic electrons using the IMPTAM-VERB coupled model. *Journal of Atmospheric and Solar-Terrestrial Physics*, *191*, 105050. https://doi.org/10.1016/j.jastp.2019.05.014Denton, R. E., Takahashi, K., Galkin, I. A., Nsumei, P. A., Huang, X., Reinisch, B. W., et al. (2006). Distribution of density along magnetospheric field lines. *Journal of Geophysical Research: Space Physics*, *111*(4), 1–13. https://doi.org/10.1029/2005JA011414Drozdov, A. Y., Shprits, Y. Y., Usanova, M. E., Aseev, N. A., Kellerman, A. C., & Zhu, H. (2017). EMIC wave parameterization in the long-term VERB code simulation. *Journal of Geophysical Research: Space Physics*, *122*(8), 8488–8501. https://doi.org/10.1002/2017JA024389Fok, M.-C., Buzulukova, N. Y., Chen, S.-H., Glocer, A., Nagai, T., Valek, P., & Perez, J. D. (2014). The Comprehensive Inner Magnetosphere-Ionosphere Model. *Journal of Geophysical Research: Space Physics*, (119), 7522–7540.Glauert, S. A., & Horne, R. B. (2005). Calculation of pitch angle and energy diffusion coefficients with the PADIE code. *Journal of Geophysical Research: Space Physics*, *110*(A4), 1–15. https://doi.org/10.1029/2004JA010851Glauert, S. A., Horne, R. B., & Mered-

ith, N. P. (2014). Simulating the Earth's radiation belts: Internal acceleration and continuous losses to the magnetopause. *Journal of Geophysical Research: Space Physics*, *119*(9), 7444–7463. https://doi.org/10.1002/2014JA020092Jahn, J.-M., Goldstein, J., Kurth, W. S., Thaller, S., de Pascuale, S. D., Wygant, J., & Reeves, G. D. (2020). Determining Plasmaspheric Density From the Upper Hybrid Resonance and From the Spacecraft Potential : How Do They Compare? *Journal of Geophysical Research : Space Physics*, *125*, 1–17. https://doi.org/10.1029/2019JA026860Jin, X., & Han, J. (2017). K-Medoids Clustering. *Encyclopedia of Machine Learning and Data Mining*, 697–700. https://doi.org/10.1007/978-1-4899-7687-1_432Kim, K. C., Shprits, Y., Subbotin, D., & Ni, B. (2011). Understanding the dynamic evolution of the relativistic electron slot region including radial and pitch angle diffusion. *Journal of Geophysical Research: Space Physics*, *116*(10). https://doi.org/10.1029/2011JA016684Kletzing, C. A., Kurth, W. S., Acuna, M. L., MacDowall, R. J., Torbert, R. B., Averkamp, T., et al. (2013). The Electric and Magnetic Field Instrument Suite and Integrated Science (EMFISIS) on RBSP. *Space Science Reviews*, *179*, 127–181. https://doi.org/10.1007/s11214-013-9993-6Landis, D. A., Saikin, A. A., Zhelavskaya, I. S., Drozdov, A. Y., Aseev, N. A., Shprits, Y. Y., et al. (2022). NARX Neural Network Derivations of the Outer Boundary Radiation Belt Electron Flux. *Space Weather*, 2–31. https://doi.org/10.1029/2021SW002774Li, W., Ni, B., Thorne, R. M., Bortnik, J., Green, J. C., Kletzing, C. A., et al. (2013). Constructing the global distribution of chorus wave intensity using measurements of electrons by the POES satellites and waves by the Van Allen Probes. *Geophysical Research Letters*, *40*(17), 4526–4532. https://doi.org/10.1002/grl.50920Malaspina, D. M., Jaynes, A. N., Boulé, C., Bortnik, J., Thaller, S. A., Ergun, R. E., et al. (2016). The distribution of plasmaspheric hiss wave power with respect to plasmapause location. *Geophysical Research Letters*, *43*(15), 7878–7886. https://doi.org/10.1002/2016GL069982Malaspina, D. M., Jaynes, A. N., Hospodarsky, G., Bortnik, J., Ergun, R. E., & Wygant, J. R. (2017). Statistical properties of low-frequency plasmaspheric hiss. *Journal of Geophysical Research: Space Physics*, *122*(8), 8340–8352. https://doi.org/10.1002/2017JA024328Malaspina, D. M., Zhu, H., & Drozdov, A. Y. (2020). A Wave Model and Diffusion Coefficients for Plasmaspheric Hiss Parameterized by Plasmapause Location. *Journal of Geophysical Research: Space Physics*, 1–23. https://doi.org/10.1029/2019ja027415Miyoshi, Y. S., Jordanova, V. K., Morioka, A., Thomsen, M. F., Reeves, G. D., Evans, D. S., & Green, J. C. (2006). Observations and modeling of energetic electron dynamics during the October 2001 storm. *Journal of Geophysical Research: Space Physics*, *111*(11), 1–12. https://doi.org/10.1029/2005JA011351Moldwin, M. B., Downward, L., Rassoul, H. K., Amin, R., & Anderson, R. R. (2002). A new model of the location of the plasmapause: CRRES results. *Journal of Geophysical Research: Space Physics*, *107*, 1–9. https://doi.org/10.1029/2001JA009211Ni, B., Cao, X., Zou, Z., Zhou, C., Gu, X., Bortnik, J., et al. (2015). Resonant scattering of outer zone relativistic electrons by multiband EMIC waves and resultant electron loss time scales. *Journal of Geophysical Research:*

Space Physics, *120*, 1–17. https://doi.org/10.1002/2015JA021466.ReceivedNi, Binbin, Cao, X., Shprits, Y. Y., Summers, D., Gu, X., Fu, S., & Lou, Y. (2018). Hot Plasma Effects on the Cyclotron-Resonant Pitch-Angle Scattering Rates of Radiation Belt Electrons Due to EMIC Waves. *Geophysical Research Letters*, *45*(1), 21–30. https://doi.org/10.1002/2017GL076028Olson, W. P., & Pfitzer, K. A. (1974). A Quantitative Model of the Magnetospheric Magnetic Field. *Journal of Geophysical Research*, *79*(25), 3739–3748. https://doi.org/10.1029/JA079i025p03739Orlova, K., Shprits, Y. Y., & Spasojevic, M. (2016). New global loss model of energetic and relativistic electrons based on Van Allen Probes measurements. *Journal of Geophysical Research: Space Physics*, *121*(2), 1308–1314. https://doi.org/10.1002/2015JA021878Orlova, Ksenia, & Shprits, Y. (2014). Model of lifetimes of the outer radiation belt electrons in a realistic magnetic field using realistic chorus wave parameters. *Journal of Geophysical Research A: Space Physics*, *119*(2), 770–780. https://doi.org/10.1002/2013JA019596Saikin, A. A., Shprits, Y. Y., Drozdov, A. Y., Landis, D. A., Zhelavskaya, I. S., & Cervantes, S. (2021). Reconstruction of the Radiation Belts for Solar Cycles 17 – 24 (1933 – 2017). *Space Weather*, *19*(e2020SW002524). https://doi.org/10.1029/2020sw002524Shprits, Y. Y., & Ni, B. (2009). Dependence of the quasi-linear scattering rates on the wave normal distribution of chorus waves. *Journal of Geophysical Research: Space Physics*, *114*(11), 1–10. https://doi.org/10.1029/2009JA014223Shprits, Y. Y., Subbotin, D. A., Meredith, N. P., & Elkington, S. R. (2008). Review of modeling of losses and sources of relativistic electrons in the outer radiation belt I: Radial transport. *Journal of Atmospheric and Solar-Terrestrial Physics*, *70*(14), 1694–1713. https://doi.org/10.1016/j.jastp.2008.06.014Shprits, Yuri Y., Thorne, R. M., Horne, R. B., & Summers, D. (2006). Bounce-averaged diffusion coefficients for field-aligned chorus waves. *Journal of Geophysical Research: Space Physics*, *111*(10), 1–6. https://doi.org/10.1029/2006JA011725Spasojevic, M., Shprits, Y. Y., & Orlova, K. (2015). Global empirical models of plasmaspheric hiss using Van Allen Probes. *Journal of Geophysical Research: Space Physics*, 370–383. https://doi.org/10.1002/2015JA021803.isSpence, H. E., Reeves, G. D., Baker, D. N., Blake, J. B., Bolton, M. K., Bourdarie, S., et al. (2013). Science goals and overview of the Radiation Belt Storm Probes (RBSP) Energetic Particle, Composition, and Thermal Plasma (ECT) suite on NASA's Van Allen Probes mission. *Space Sci Rev*, (179), 311–336. https://doi.org/10.1007/s11214-013-0007-5Subbotin, D. A., & Shprits, Y. Y. (2009). Three-dimensional modeling of the radiation belts using the versatile electron radiation belt (verb) code. *Space Weather*, *7*(10), 1–15. https://doi.org/10.1029/2008SW000452Subbotin, D. A., & Shprits, Y. Y. (2012). Three-dimensional radiation belt simulations in terms of adiabatic invariants using a single numerical grid. *Journal of Geophysical Research: Space Physics*, *117*(5), 1–12. https://doi.org/10.1029/2011JA017467Subbotin, D. A., Shprits, Y. Y., & Ni, B. (2011). Long-term radiation belt simulation with the VERB 3-D code: Comparison with CRRES observations. *Journal of Geophysical Research: Space Physics*, *116*(12), 1–14.

https://doi.org/10.1029/2011JA017019Subbotin, D. A., Shprits, Y. Y., Gkioulidou, M., Lyons, L. R., Ni, B., Merkin, V. G., et al. (2011). Simulation of the acceleration of relativistic electrons in the inner magnetosphere using RCM - VERB coupled codes. *Journal of Geophysical Research*, *116*, 1–12. https://doi.org/10.1029/2010JA016350Summers, D., Ni, B., & Meredith, N. P. (2007). Timescales for radiation belt electron acceleration and loss due to resonant wave-particle interactions. *Journal of Geophysical Research: Space Physics*, *112*, 1–11. https://doi.org/10.1029/2006JA011801Tsurutani, B. T., Falkowski, B. J., Pickett, J. S., Santolik, O., & Lakhina, G. S. (2015). Plasmaspheric hiss properties: Observations from Polar. *Journal of Geophysical Research: Space Physics*, *120*(1), 414–431. https://doi.org/10.1002/2014JA020518Wygant, J. R., Bonnell, J. W., Goetz, K., Ergun, R. E., Mozer, F. S., Bale, S. D., et al. (2013). The Electric Field and Waves Instruments on the Radiation Belt Storm Probes mission. *Space Sci Rev*, 183–220. https://doi.org/10.1007/978-1-4899-7433-4-6Zhang, J.-C., Halford, A. J., Saikin, A. A., Huang, C.-L., Spence, H. E., Larsen, B. A., et al. (2016). EMIC waves and associated relativistic electron precipitation on 25-26 January 2013. *Journal of Geophysical Research: Space Physics*, *121*, 1–15. https://doi.org/10.1002/2015JA021023.ReceivedZhu, H., Shprits, Y. Y., Spasojevic, M., & Drozdov, A. Y. (2019). New hiss and chorus waves diffusion coefficient parameterizations from the Van Allen Probes and their effect on long-term relativistic electron radiation-belt VERB simulations. *Journal of Atmospheric and Solar-Terrestrial Physics*, *193*. https://doi.org/10.1016/j.jastp.2019.105090